



**Please cite the Published Version**

Shi, X , Liu, M, He, P, Chen, J, Beake, BD, Liskiewicz, TW  and Chen, J (2024) Plasma-sprayed high entropy alloy coating with novel MoS<sub>2</sub>/resin hybrid sealant: tribological and corrosion characterization. *Ceramics International*, 50 (22, A). pp. 45763-45775. ISSN 0272-8842

**DOI:** <https://doi.org/10.1016/j.ceramint.2024.08.417>

**Publisher:** Elsevier BV

**Version:** Accepted Version

**Downloaded from:** <https://e-space.mmu.ac.uk/636518/>

**Usage rights:**  [Creative Commons: Attribution 4.0](https://creativecommons.org/licenses/by/4.0/)

**Additional Information:** This is an author-produced version of the published paper, which appeared in *Ceramics International*, published by Elsevier. Uploaded in accordance with the University's Research Publications Policy.

**Enquiries:**

If you have questions about this document, contact [openresearch@mmu.ac.uk](mailto:openresearch@mmu.ac.uk). Please include the URL of the record in e-space. If you believe that your, or a third party's rights have been compromised through this document please see our Take Down policy (available from <https://www.mmu.ac.uk/library/using-the-library/policies-and-guidelines>)

# Plasma-sprayed high entropy alloy coating with novel MoS<sub>2</sub>/resin hybrid sealant: Tribological and corrosion characterization

Xiangru Shi<sup>a\*</sup>, Ming Liu<sup>a</sup>, Peihua He<sup>a</sup>, Jian Chen<sup>b</sup>, Ben D. Beake<sup>c</sup>, Tomasz W. Liskiewicz<sup>d</sup>, Jiangbo Chen<sup>a</sup>

a. School of Materials Science and Engineering, Hohai University, Nanjing 210098, China

b. School of Materials Science and Engineering, Jiangsu Key Laboratory for Advanced Metallic Materials, Southeast University, Nanjing 211189, China

c. Micro Materials Ltd., Willow House, Yale Business Village, Ellice Way, Wrexham, LL13 7YL, UK

d. Faculty of Science and Engineering, Manchester Metropolitan University, Dalton Building, Chester Street, Manchester M15 6BH, UK

\* Corresponding author. E-mail address: [sxr12009210@163.com](mailto:sxr12009210@163.com) (Xiangru Shi)

## Abstract

Sealing treatment provides a strategy for the long-term performance of thermal spray coatings under actual working conditions. However, common sealants are mainly limited to improving the corrosion resistance of coatings, neglecting applications in more complex environments where they are subject to simultaneous corrosion and wear. Herein, a novel organic-inorganic hybrid composite sealant, composed of self-lubricating MoS<sub>2</sub> nanoparticles and environmentally friendly waterborne silicone modified acrylic resin (WBS-ACR), was successfully prepared in the pores and micro-defects of plasma-sprayed HEA coatings by one-step hydrothermal method. The results indicate that MoS<sub>2</sub> nanosheets are uniformly synthesized in resin materials through precursor hydrothermal reactions. The hybrid sealants are filled densely in the micro-defects of HEA coatings with a maximum penetration depth greater than 180 μm. The tribological and electrochemical results indicate that the hybrid sealant exhibits similar anti-wear performance, but two orders of magnitude lower corrosion currents than that of pure MoS<sub>2</sub> sealant. In comparison to the pure resin sealant, the hybrid sealant retains its excellent corrosion resistance while increasing its wear resistance. The superior comprehensive performance of the novel organic-inorganic hybrid sealant could expand the application of thermal spray coatings into new fields.

**Keywords:** HEA coatings, hybrid sealants, anti-wear performance, corrosion resistance

## 1. Introduction

Recently, high-entropy alloys (HEAs), composed of at least five principal elements in equimolar or near-equimolar ratios, have attracted great attention due to their combination of high hardness, high temperature oxidation resistance, wear resistance and corrosion resistance[1-3]. In comparison to HEA bulk materials, HEA coatings can ensure efficient utilization of their performance characteristics while significantly reducing the preparation cost and shortening the preparation cycle of HEAs, thus having greater potential in engineering application. HEA coatings can be produced by a range of preparation methods such as laser cladding, plasma cladding, magnetron sputtering and thermal spray technologies [4-7]. Among them, thermal spray technology has more advantages for industry due to its convenient operation, simplified equipment and high production efficiency. However, pores and micro-defects will inevitably appear in the HEA coatings due to the layered stacking of completely or partially unmelted particles during the thermal spray process[3-5]. The complex structural defects in the HEA coatings not only affect the mechanical properties, wear resistance and other properties, but also provide the transportation channels for the corrosive media such as air, water, ions, etc., seriously restricting the service stability and life of the equipment.

Fortunately, the sealing treatment with sealants provides a technical and economic solution for actual production[8-12]. By simple immersion and ultrasonic excitation, the sealant material can penetrate into the pores of the coating, which not only reduces the porosity of the coating, but also endows the coating with excellent corrosion resistance and wear resistance. Among various sealing materials, organic resin-based sealants are the most commonly used and effective method for adjusting the structural defects and corrosion resistance of thermal spray coatings[10-12]. For example, Tian *et al.*[10] studied the failure behavior of HVOF sprayed WC-10Co4Cr sealed with epoxy resin in artificial seawater finding that the sealant significantly improved the corrosion and cavitation resistance of the as-sprayed coatings. Zhang *et al.*[11] found that the corrosion current density of the Cr<sub>2</sub>O<sub>3</sub>-8TiO<sub>2</sub> coating sealed with organic silicone resin sealant decreased by more than an order of magnitude compared to the unsealed coating, and decreased by about 40% compared to the epoxy resin sealing coating. However, organic resin sealants have the problems of poor mechanical properties and wear resistance, which limits their application in extreme conditions.

The introduction of various functional nano-fillers into polymers provides an effective strategy for improving the tribological properties. For example, MoS<sub>2</sub> is composed of sandwich lamellar structure and has been extensively studied in various applications due to its desirable wear and corrosion resistance[13-15] Some studies have reported

improved tribological properties of thermal sprayed coatings using MoS<sub>2</sub> as a sealing material [16-20]. Deng *et al.*[19,20] synthesized MoS<sub>2</sub> nanoparticles in the pores and micro-cracks of plasma-sprayed ZrO<sub>2</sub> coating by in-situ hydrothermal method. The MoS<sub>2</sub> nanoparticles increased the tribological properties significantly. Li *et al.*[18] investigated the influence of MoS<sub>2</sub> nano-fillers on the tribological performance of yttria-stabilized zirconia (YSZ) coating by hydrothermal reaction. The YSZ/MoS<sub>2</sub> composite coatings showed extremely long lifetime and low friction. As mentioned above, the combination of an organic resin with inorganic MoS<sub>2</sub> nanoparticles as sealing materials has the potential to take full advantage of their superior corrosion resistance and tribological performance, respectively.

Many efforts have been made to incorporate the MoS<sub>2</sub> into polymer matrices to prepare organic/inorganic hybrid materials [21-26]. According to reports, many properties have been significantly improved, including mechanical properties, fire resistance, wear resistance, and corrosion resistance. Zhou *et al.*[26] found that the thermal stability of polymethyl methacrylate (PMMA) can be significantly improved by adding only 1% MoS<sub>2</sub> through a facile emulsion polymerization method. Xia *et al.*[24] successfully combined polydopamine (PDA) modified MoS<sub>2</sub> with epoxy resin coatings and found that its corrosion resistance was three orders of magnitude higher than that of uncombined coatings. Lin *et al.*[23] introduced Si<sub>3</sub>N<sub>4</sub>@MoS<sub>2</sub> core-shell hybrid particles (CSs) into epoxy resin/polyacrylate IPN organic matrix in three steps to form a composite coating. The CSs improved the corrosion resistance and tribological properties of IPN organic matrix due to the self-lubrication and shielding effect of MoS<sub>2</sub>. These studies have mainly concentrated on the reinforcement properties of composite materials themselves. Few of them have been focused on its possible use as a sealing material to improve the corrosion and tribological properties of thermal sprayed coatings. Moreover, in most studies MoS<sub>2</sub> was compounded directly with resin matrices through simple mechanical mixing, which inevitably leads to serious aggregation of MoS<sub>2</sub> in resin due to the surface energy difference. Therefore, a new approach to prepare the MoS<sub>2</sub>/resin composite is needed.

In this paper, the waterborne silicone modified acrylic resin (WBS-ACR) was used as the polymer matrix due to its water solubility, non-toxicity, and high temperature resistance. Sodium molybdate and thiourea was chosen as the precursor to prepare the MoS<sub>2</sub> layered nano-filler. Subsequently, the MoS<sub>2</sub>/WBS-ACR hybrid sealant was prepared *in situ* in the pores and micro-defects of plasma-sprayed HEA coatings by one-step hydrothermal method. The microstructure and composition of the MoS<sub>2</sub>/WBS-ACR powders and MoS<sub>2</sub>/WBS-ACR@HEA coatings were studied. Afterward, the

corrosion resistance and tribological properties of the MoS<sub>2</sub>/WBS-ACR@HEA coatings were investigated and compared with the as-sprayed HEA coating, MoS<sub>2</sub>@HEA coating and WBS-ACR@HEA coating. The corrosion and tribological mechanism of the WBS-ACR@HEA coating is discussed. The preliminary results obtained will be helpful for the application of thermal spraying coatings in extreme working conditions.

## 2. Experimental Section

### 2.1 Materials

Waterborne silicone modified acrylic resin (WBS-ACR) was purchased from Qingdao Jinwanli Fine Chemical Co., Ltd. Thiourea (CH<sub>4</sub>N<sub>2</sub>S) and sodium molybdate (Na<sub>2</sub>MoO<sub>4</sub>) were provided by Shanghai Maclean Reagent Co., Ltd. The defoaming agent (BYK024), dispersing agent (BYK156) and activating agent (BYK346) were supplied by BYK Additives Co., Ltd. Deionized water was homemade using a water purification system. High-entropy alloy powder (FeCoCrNiAl, 45-105 μm) was purchased from Shandong Lianhong New Material Technology Co. Ltd., and its composition is listed in Table 1.

**Table 1.** The composition of the high-entropy alloy powder.

Elements	Fe	Co	Ni	Cr	Al	other
Chemical composition (wt%)	21.82	23.62	23.21	20.46	10.84	0.05

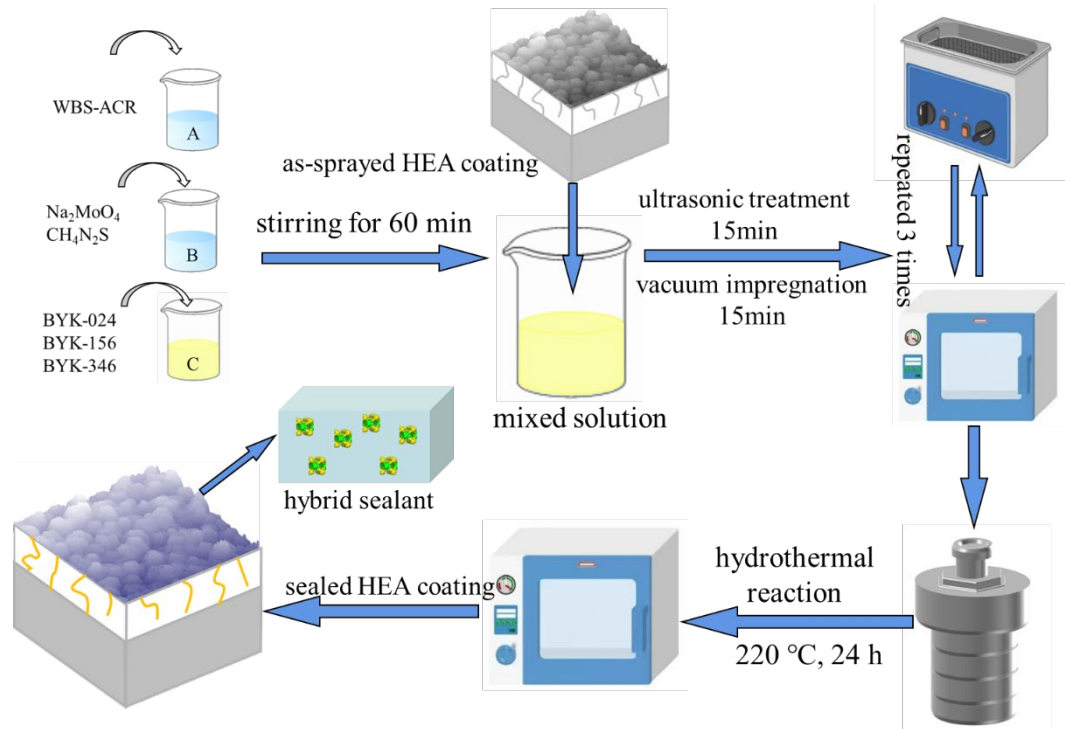
### 2.2 Preparation of HEA coatings

An atmospheric plasma spraying system (Praxair 3710) was used to prepare the HEA coatings with the commercial high-entropy alloy powder. The target coating with thickness of about 300 μm was deposited on Q235 steel substrate with the parameters shown in Table 2. Before deposition, the spraying surfaces of the substrate were sand-blasted to increase the roughness and adhesion strength between the coating and substrate. Then the substrates were ultrasonic cleaned in ethanol and acetone for 20 min, respectively. After deposition, the coating was cut into the dimension of 10 mm×10 mm×5 mm, and then cleaned ultrasonically in deionized water, ethanol and acetone in sequence for 20 min each.

**Table 2.** Atmospheric plasma spraying parameters

Parameters	Current (A)	Voltage (V)	Primary gas (Ar) (psi)	Carrier gas (Ar) (psi)	Spraying distance (mm)
Value	700	50	75	100	150

### 2.3 Preparation of $\text{MoS}_2/\text{WBS-ACR}@\text{HEA}$ coating

**Fig. 1.** The schematic diagram of the preparation of  $\text{MoS}_2/\text{WBS-ACR}@\text{HEA}$  coating

The  $\text{MoS}_2/\text{WBS-ACR}$  hybrid sealant was prepared *in situ* in the pores and micro-defects of plasma-sprayed HEA coatings by a one-step hydrothermal method. Firstly, three kinds of solutions were prepared before the experiment: 20 g of WBS-ACR was dissolved in 60 ml of deionized water accompanied by mechanical stirring for 30 min to form solution A; 0.8 g  $\text{Na}_2\text{MoO}_4$  and 0.887 g  $\text{CH}_4\text{N}_2\text{S}$  was added into 20 ml of deionized water with vigorous stir for 5 min to form solution B; 3 drops of BYK024, BYK156, and BYK346 each were mixed into 2 ml of deionized water to form solution C. Next, the three solutions A, B and C were mixed together and stirred strongly for another 60 min. After that, the post-treated coatings were immersed in the well stirred solution for ultrasonic treatment for 15 min, and then placed in a vacuum chamber and held at 0.09 MPa for another 15 min. To ensure that the precursor solution penetrates as much as possible into the pores of the coating, the above step was repeated three times. Subsequently, the mixture with the coatings were transferred into a 150 ml Teflon

lined autoclave for 24 h at 220 °C. After cooling naturally to room temperature, the specimens were taken out to remove the excess product on the surface of the HEA coating, while the other precipitates were also collected and dried at 60 °C for 12 h. For the sake of contrast, the MoS<sub>2</sub>@HEA coating was also prepared based on the above steps without solution A and C, while the WBS-ACR@HEA coating was prepared without solution B and C. The schematic diagram of the preparation of MoS<sub>2</sub>/WBS-ACR@HEA coating is shown in Fig.1.

**Table 3.** The abbreviation of the tested samples.

<b>Coating</b>	<b>Composition</b>
HEA	High entropy alloy (HEA) coating
MoS <sub>2</sub> @HEA	HEA coating sealed with MoS <sub>2</sub>
WBS-ACR@HEA	HEA coating sealed with waterborne silicone acrylic resin
MoS <sub>2</sub> /WBS-ACR@HEA	HEA coating sealed with waterborne silicone acrylic resin and MoS <sub>2</sub>

## **2.4 General characterization**

The morphologies and microstructures of the as-synthesized sealant powders and as-sealed coatings were observed by scanning electron microscopy (SEM, FEI XL-30, USA) at 20.0 KV, in which the elemental composition was analyzed by energy dispersive spectroscopy (EDS). X-ray diffraction (XRD, Bruker D2 Phaser, Germany) was performed to analyze phase composition of the synthetic powders in the 2θ range of 5-80° with copper Kα radiation. Fourier transform infrared spectrum (FTIR, Thermo Scientific Nicolet iS20, USA) was acquired to confirm the composition of the synthesized sealants in the wavenumber range of 400-4000 cm<sup>-1</sup>. All the sealant powders were mixed with KBr powder and pressed into tablets for characterization. Further, the X-ray photoelectron spectroscopy (XPS, Thermo Scientific K-Alpha, USA) was conducted to measure the element and bonding state of the MoS<sub>2</sub>/WBS-ACR nanocomposites with monochromatic AlKα irradiation, while the transmission electron microscopy (TEM, FEI Talos 200S, USA) was employed to investigate more details on the micro-morphology of MoS<sub>2</sub>/WBS-ACR nanocomposites at an accelerating voltage of 200 keV.

## **2.5 Corrosion and tribological behavior tests**

In order to study the corrosion resistance of the coatings, the potentiodynamic polarization and electrochemical impedance spectroscopy (EIS) were tested in 3.5 wt% NaCl solution using a CHI660E electrochemical setup (CH Instruments Ins. USA). A

classical three-electrode cell arrangement was used, in which the coatings, Ag/AgCl electrode and a platinum sheet were used as the working electrode, reference electrode and counter electrode, respectively. The scanning potential range of the potentiodynamic polarization curve was set from -1.5 V to 0.5 V at a scanning rate of 0.5 mV/s. The EIS were conducted in the frequency range from 0.01 Hz to 100 kHz. All the tests were started after immersing the samples in 3.5 wt% NaCl solution for 60 min to obtain stable open circuit potentials (OCP).

The tribological properties of the coatings were evaluated at ambient temperature and atmospheric environment using a ball-on-disc rotary tribometer. The frictional counterparts were ZrO<sub>2</sub> ceramic balls with a diameter of 5 mm due to their good wear resistance and high hardness. All the friction tests were carried out under the applied load of 5 N, rotation speed of 180 r/min, rotation radius of 3 mm, and the test duration of 60 min. To investigate the repeatability of the obtained friction coefficient measurements, each sample was tested three times at different locations. After the friction tests, the wear morphologies of the coatings were observed by SEM (SN3400, Hitachi, Japan), while the wear volume ( $V$ ) was measured by the white light interferometer (HST-200, RTEC, USA). The specific wear rate ( $W$ ) was calculated by the formula:  $W=V/FL$ , where  $F$  is the applied load and the  $L$  is the sliding distance.

### **3. Results and Discussion**

#### ***3.1 Characterization of the synthetic sealant powders***

The microstructure and morphologies of the synthesized MoS<sub>2</sub> and MoS<sub>2</sub>/WBS-ACR composite powders were studied by SEM and TEM, as shown in Fig.2. As can be seen from Fig. 2a, the as-prepared MoS<sub>2</sub> is freely assembled from many ultrathin petal-like nanosheets, in which loose nanopores were surrounded by the interconnection nanoflakes. This result is consistent with the hydrothermal synthesis of MoS<sub>2</sub> reported previously [18, 19]. When the WBS-ACR is incorporated to prepare MoS<sub>2</sub>/WBS-ACR nanocomposite (Fig. 2b), the MoS<sub>2</sub> is completely encased in a polymer matrix, and the morphology features of petal-like nanosheets could be seen ambiguously from the surface of the composite powder. In addition, no evidence of any obvious agglomeration was found in Fig. 2b, since MoS<sub>2</sub> was generated through the reaction of precursor solution in the polymer matrix. To further analyze the dispersion of MoS<sub>2</sub> in resin matrix, the TEM images of the MoS<sub>2</sub>/WBS-ACR composite are shown in Fig. 2(c, d). It can be clearly seen that the MoS<sub>2</sub> sheets are randomly dispersed in the WBS-ACR. The sheets show the typical MoS<sub>2</sub> lamellar structure with parts of ordered aggregation. The appearance of C, Mo and S elements in the EDS mapping of the MoS<sub>2</sub>/WBS-ACR



composite (Fig. 2e) also demonstrates the successful synthesis and uniform distribution of MoS<sub>2</sub> in the WBS-ACR matrix.

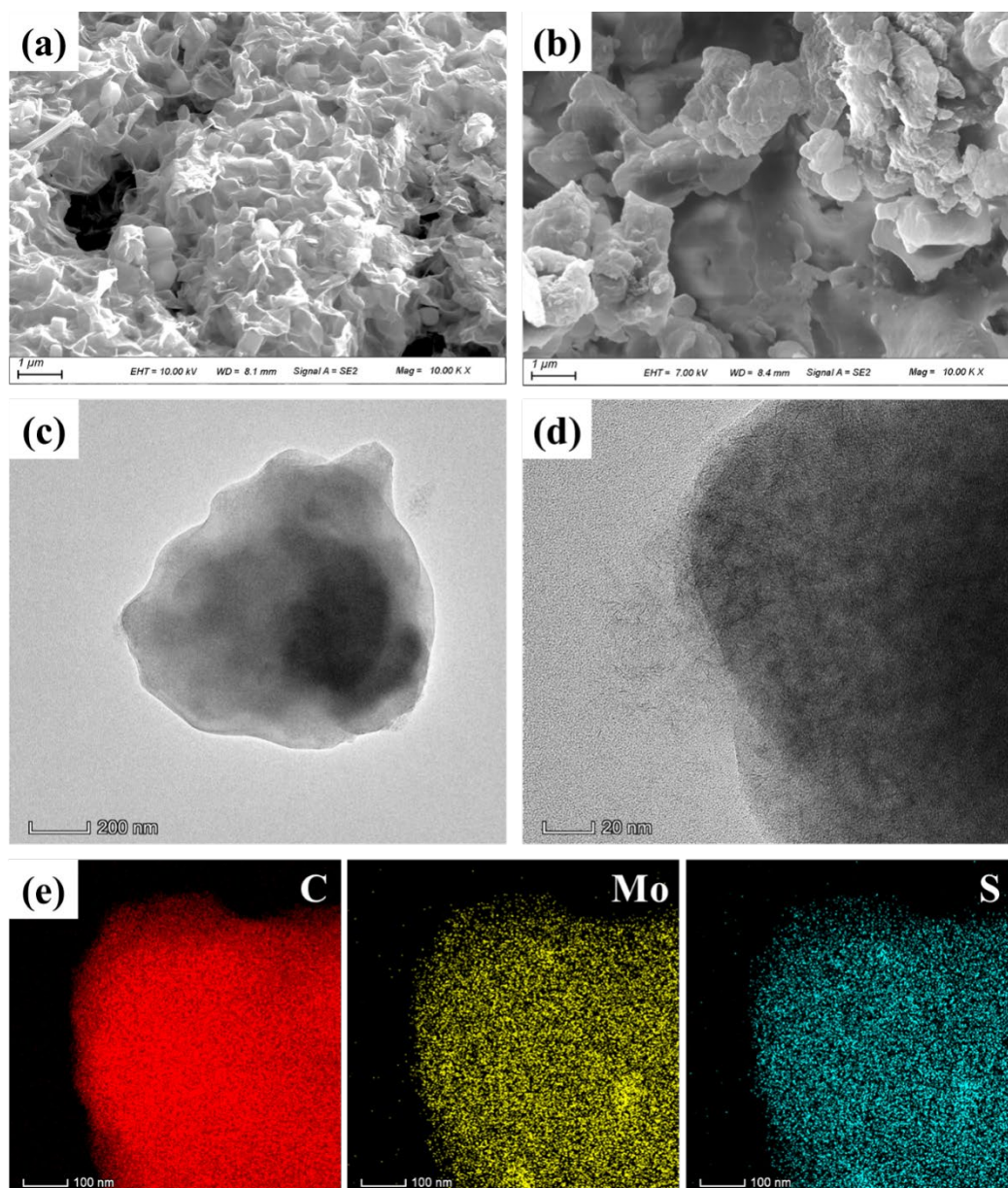


**Fig. 2.** SEM images of (a) MoS<sub>2</sub> powder, (b) MoS<sub>2</sub>/WBS-ACR composite powder; (c, d) TEM image of MoS<sub>2</sub>/WBS-ACR composite powder and (e) the corresponding EDS element mapping.

The crystalline phase and structure of the as-prepared MoS<sub>2</sub>, WBS-ACR and MoS<sub>2</sub>/WBS-ACR composite powders was investigated by using XRD spectroscopy, as shown in Fig. 3a. It could be observed that there existed five clear characteristic peaks of MoS<sub>2</sub> powder at 11.6°, 18.8°, 28.6°, 32.2°, 57.6°, which is consistent with that of 1T-MoS<sub>2</sub> [27-30]. The diffraction peaks located at 2θ of 32.2° and 57.6° is corresponding to the typical (100) and (110) crystal planes of MoS<sub>2</sub>. The characteristic peak (002) of

MoS<sub>2</sub> shifts from regular 14.3° to 11.6° indicating the expanded interlayer spacing. The XRD peaks located at about 18.8° and 28.6° can be indexed as the (004) peak of MoS<sub>2</sub> [28, 29]. The virgin WBS-ACR powder exhibits a broad crystalline peak at around 10°-25°, due to its amorphous crystalline structure. For the MoS<sub>2</sub>/WBS-ACR nanocomposite, the characteristic peaks of both MoS<sub>2</sub> and WBS-ACR can be observed in the XRD curve, which demonstrates that the MoS<sub>2</sub> was successfully *in situ* grown in the WBS-ACR matrix. Besides, it is worth noting that the diffraction peaks of MoS<sub>2</sub> located at 32.2° (100) and 57.6° (110) becomes extremely weak and broad, while the other diffraction peaks disappeared directly in the WBS-ACR matrix. This phenomenon could be attributed to the disordered stacking of MoS<sub>2</sub> and the shielding effect of WBS-ACR, which is in good agreement with the TEM results.

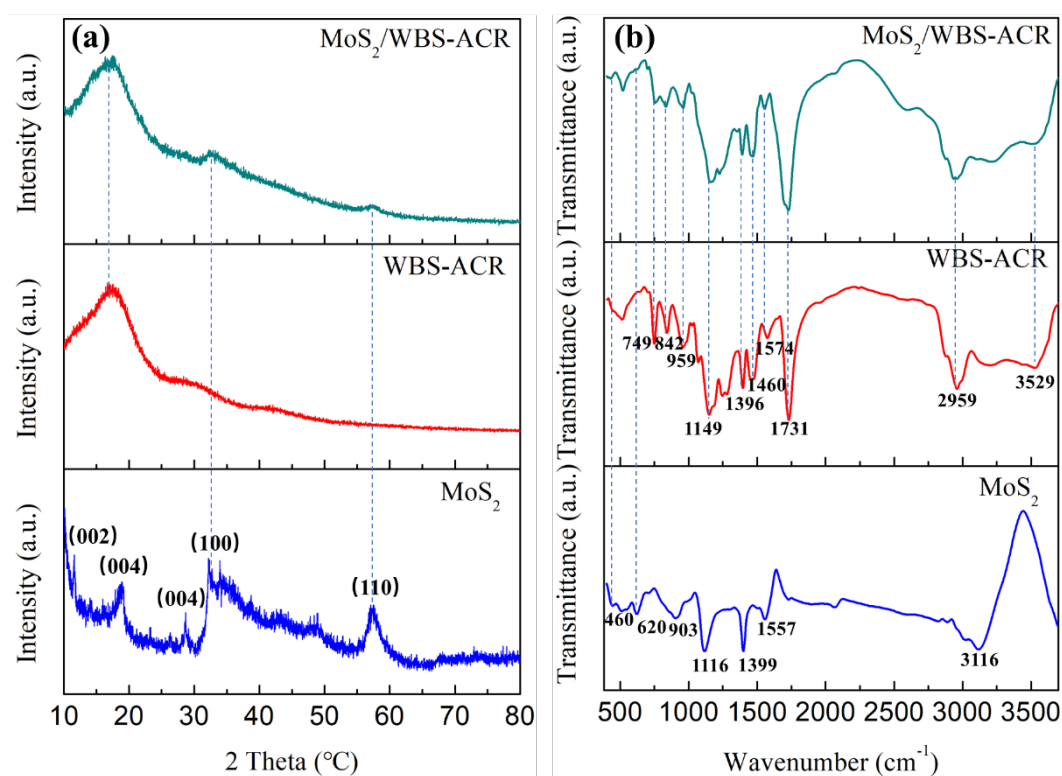


**Fig. 3.** (a) XRD and (b) FTIR spectra of as-prepared MoS<sub>2</sub>, WBS-ACR and MoS<sub>2</sub>/WBS-ACR composite powders.

Fourier transform infrared spectroscopy (FTIR) is also an effective technique for confirming the composition of the synthesized samples. Fig. 3b shows the FTIR spectra of the as-prepared MoS<sub>2</sub>, WBS-ACR and MoS<sub>2</sub>/WBS-ACR composite powders. For the pure MoS<sub>2</sub>, the typical characteristic absorption bands at 460 cm<sup>-1</sup> and 620 cm<sup>-1</sup> are corresponding to the stretching vibration and bending vibration of S-Mo-S, respectively [31, 32]. The bands at 1116 cm<sup>-1</sup> and 1399 cm<sup>-1</sup> are attributed to S=O stretching vibration caused by surface oxidation when the sample comes into contact with air [33,

34]. Peaks at  $1557\text{ cm}^{-1}$  and  $3116\text{ cm}^{-1}$  correspond to stretching vibrations of -OH groups in the surface of  $\text{MoS}_2$  [24]. For the spectrum of WBS-ACR, the absorption band at around  $3529$  is related to the -OH stretching vibrations. The bands at  $2959\text{ cm}^{-1}$  and  $1396\text{ cm}^{-1}$  are associated with the stretching vibration and bending vibration of C-H in methyl groups. Peaks at  $1731\text{ cm}^{-1}$  and  $1574\text{ cm}^{-1}$  are the characteristic absorption peaks of C=O. The characteristic peak at  $1460\text{ cm}^{-1}$  originates from the bending vibration of C-H in methylene groups. Peaks at  $1149\text{ cm}^{-1}$  and  $959\text{ cm}^{-1}$  correspond to the stretching vibration of C-O-C and Si-O-Si, respectively. The bands at  $842\text{ cm}^{-1}$  and  $749\text{ cm}^{-1}$  are associated with Si-C skeleton vibrations [35, 36]. It is evident that the FTIR spectrum of  $\text{MoS}_2/\text{WBS-ACR}$  nanocomposite not only exhibits characteristic signals similar to WBS-ACR, but also possesses typical  $\text{MoS}_2$  characteristic peaks near  $460\text{ cm}^{-1}$  and  $620\text{ cm}^{-1}$ . To some extent, this result also proves that  $\text{MoS}_2$  was successfully incorporated into the WBS-ACR matrix through *in situ* hydrothermal method.

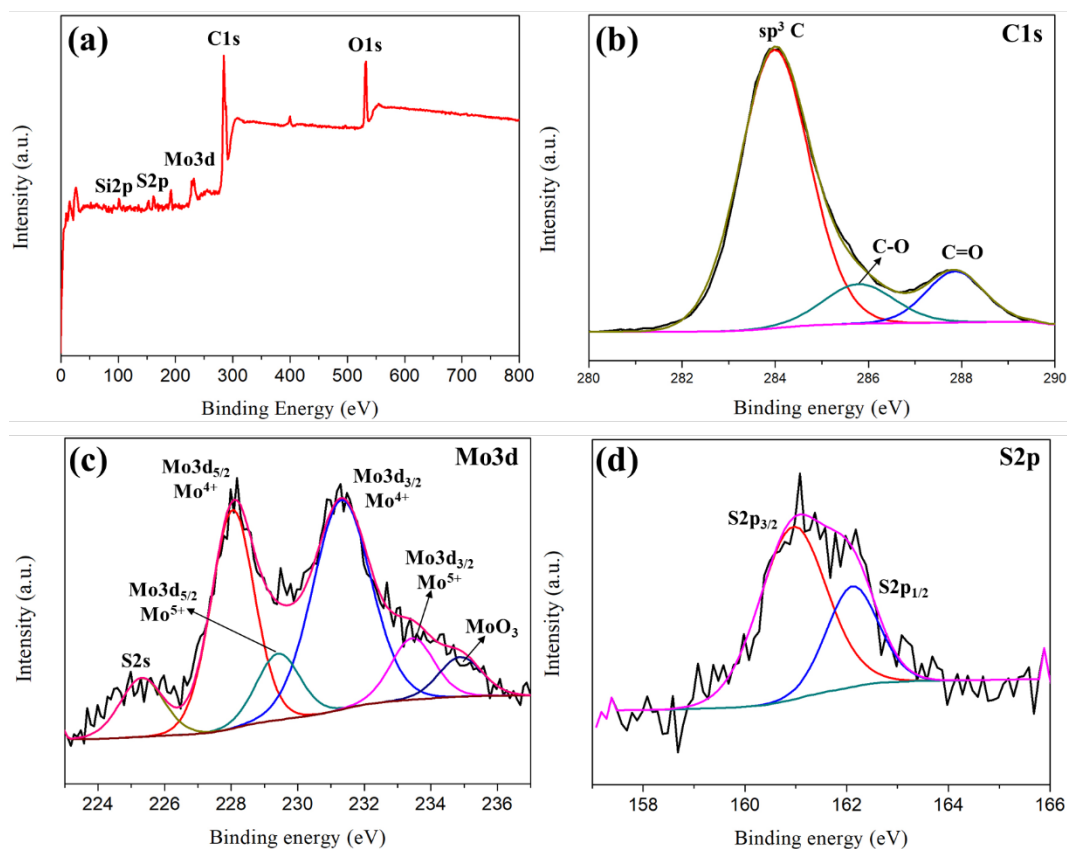


**Fig. 4.** XPS spectra of the  $\text{MoS}_2/\text{WBS-ACR}$  composite powder.

XPS was used to identify the chemical composition and atomic valence of  $\text{MoS}_2/\text{WBS-ACR}$  nanocomposite. As shown in Fig. 4a, the elements of C, Si, O, Mo and S appear in the survey spectrum of  $\text{MoS}_2/\text{WBS-ACR}$  composite powder, which also provides preliminary confirmation that the  $\text{MoS}_2$  and WBS-ACR were successfully combined.

Moreover, the narrow scans of C1s, Mo3d and S2p in MoS<sub>2</sub>/WBS-ACR composite powder were fitted by Gaussian-Lorentzian function for further proof. In the C 1s spectrum, there are three different characteristic peaks at around 283.9 eV, 285.8 eV and 287.9 eV, corresponding to the sp<sup>3</sup> bonds (C-C, C-H, C-Si etc.), C-O bond and C=O bond, respectively. Three different atomic valences were observed in the high-resolution spectrum of Mo 3d (Fig. 4c). Two strong characteristic peaks at 228.1 eV and 231.3 eV are assigned to the binding energy of Mo 3d<sub>5/2</sub> and Mo 3d<sub>3/2</sub> of Mo<sup>4+</sup> in MoS<sub>2</sub>. The double peaks occurred at around 229.4 eV and 233.4 eV are attributed to Mo<sup>5+</sup> resulting from oxysulfide intermediate phases. The peak value at 234.9 eV corresponds to Mo<sup>6+</sup>, indicating the probable formation of MoO<sub>3</sub> [13, 18, 23]. Similarly, the S 2p spectrum (Fig. 4d) shows two feature peaks at around 160.9 eV and 162.1 eV, representing the binding energy of S 2p<sub>3/2</sub> and s 2p<sub>1/2</sub> of S<sup>2-</sup> in MoS<sub>2</sub> [32, 34]. The analysis above confirms the successful preparation of MoS<sub>2</sub> in WBS-ACR matrix.

### ***3.2 Characterization of HEA coatings with sealing treatment***

In order to investigate the permeability of the as-prepared sealants, the surface, cross-sectional morphology, and corresponding EDS mapping spectra of HEA coatings treated with different sealants are shown in Fig. 5. The as-sprayed HEA coatings show features typical for plasma sprayed coatings [37, 38]. Innumerable pores with diameters ranging from a few micrometers to tens of micrometers are randomly distributed on the surface and cross-section of the HEA coatings. Microcracks with radial orientation relative to the pores can also be observed, which originated from the difference in size and flight speed of the HEA powders during the plasma spraying [39]. The existence of micro-cracks and pores will seriously adversely affect the service life of HEA coatings in harsh environments, by providing a transport channel for corrosive media such as water and chloride ions to destroy the metal substrate.

After sealing treatments, the surface morphologies (Fig. 5(a-c)) of HEA coatings become quite different. The vast majority of the open pores were completely filled with different sealants, indicating the excellent fluidity and permeability [9,40,41]. From the partially enlarged image in Fig. 5a, it can be seen that the surface of the pure MoS<sub>2</sub> filling layer is relatively rough and has obvious defects and pores due to the loose petal-like structures stacked together (Fig. 2a). However, the filling layers in Fig. 5b&c show smooth and compact microstructure, and good adhesion to the HEA coatings, demonstrating the WBS-ACR and MoS<sub>2</sub>/WBS-ACR sealants can effectively block the diffusion of corrosive media. Fig. 5(d-f) shows the cross-sectional images of the sealed HEA coatings with different sealants. Similarly, it can be observed that the sealing effect of WBS-ACR and MoS<sub>2</sub>/WBS-ACR is significantly better than that of pure MoS<sub>2</sub>, and



no obvious micro-cracks propagate along the surface of filling layers. The EDS mapping images in Fig. 5(g-i) indicate the composition the corresponding sealants. The detection of C, Mo and S elements in the coating defects (Fig. 5f) declare the successful preparation of MoS<sub>2</sub>/WBS-ACR composite sealant in the pores by one step *in-situ* hydrothermal method. Besides, the volume fraction of pores for the as-sprayed HEA coating and as-sealed HEA coatings have been statistically analyzed using ImageJ software as shown in Table. 4. The results showed that the porosity of HEA coating was significantly reduced after sealing treatment. Further, Fig. 6 shows that the penetration depth of the sealants exceeds 180 μm in the coating, which is much deeper than reported in previous studies [42-44].

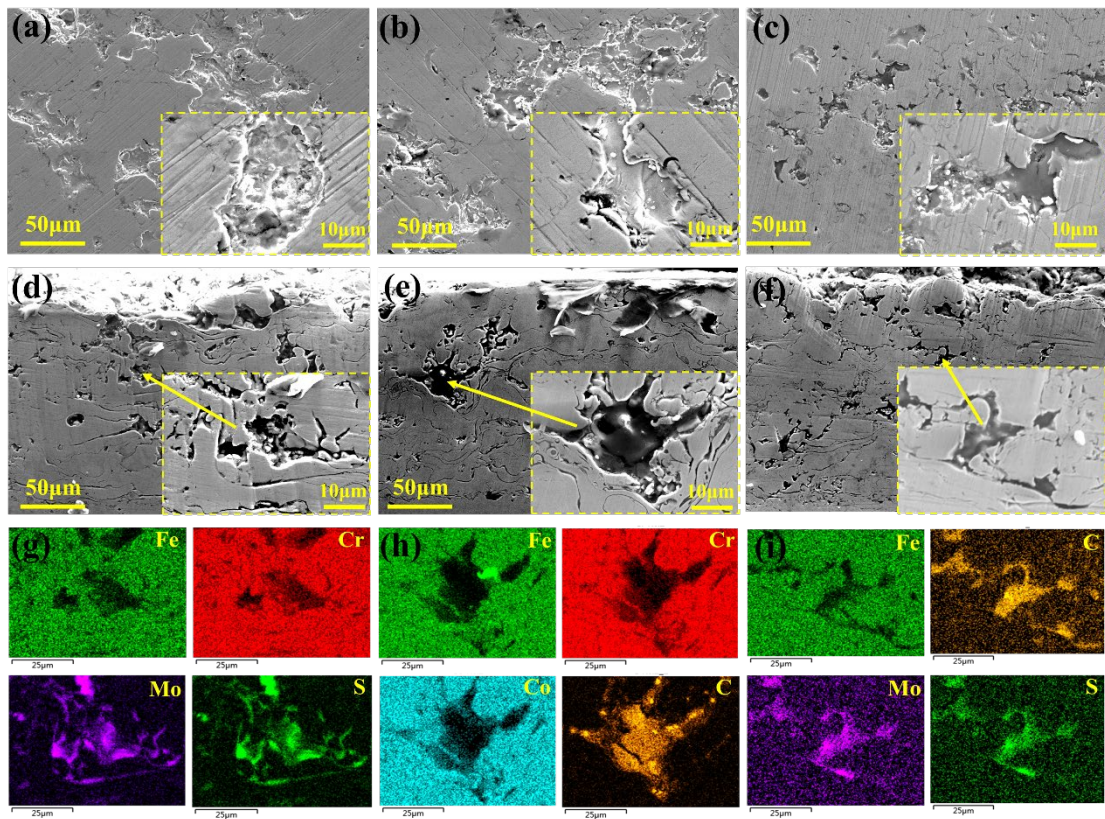


**Fig.5.** SEM images of surface, cross-sectional morphologies and the corresponding EDS mapping images of (a, d, g) MoS<sub>2</sub>@HEA coating, (b, e, h) WBS-ACR@HEA coating and (c, f, i) MoS<sub>2</sub>/WBS-ACR@HEA coating.

**Table 4.** The volume fractions of pores for the tested samples.

Samples	HEA	MoS <sub>2</sub> @HEA	WBS- ACR@HEA	MoS <sub>2</sub> /WBS- ACR@HEA
Porosity %	5.50±0.12	1.85±0.05	2.20±0.15	1.25±0.05

The principle of hydrothermal synthesis of MoS<sub>2</sub> by the reaction of sodium molybdate and H<sub>2</sub>S produced by the hydrolysis of thiourea has been widely reported [13, 18, 19, 21]. When the HEA coatings are placed in the reaction solution, the sodium molybdate and thiourea can easily penetrate into the pores and micro-defects of the coating through repeated ultrasonic and vacuum impregnation. During the hydrothermal process, thiourea will preferentially hydrolyze to produce gases such as H<sub>2</sub>S, CO<sub>2</sub> and NH<sub>3</sub>, and then Na<sub>2</sub>MoO<sub>4</sub> stored in the pores will react with the H<sub>2</sub>S to produce MoS<sub>2</sub>. Finally, a large amount of MoS<sub>2</sub> nanoparticles accumulate to form petal-like stacked structures. However, when the WBS-ACR was introduced to precursor solution, the Na<sub>2</sub>MoO<sub>4</sub> and CS(NH<sub>2</sub>)<sub>2</sub> could be first uniformly wrapped in resin with the help of surfactants, and then penetrate into the coating pores based on the good flow characteristics of the resin. Due to the constraints of surrounding resin, the produced MoS<sub>2</sub> cannot move freely to agglomerate, and can only be randomly dispersed in the WBS-ACR with fewer layers (Fig. 2d). In addition, the pressure in the reactor will increase rapidly during the hydrothermal heating process, which will promote resin penetration into deeper coating pores.

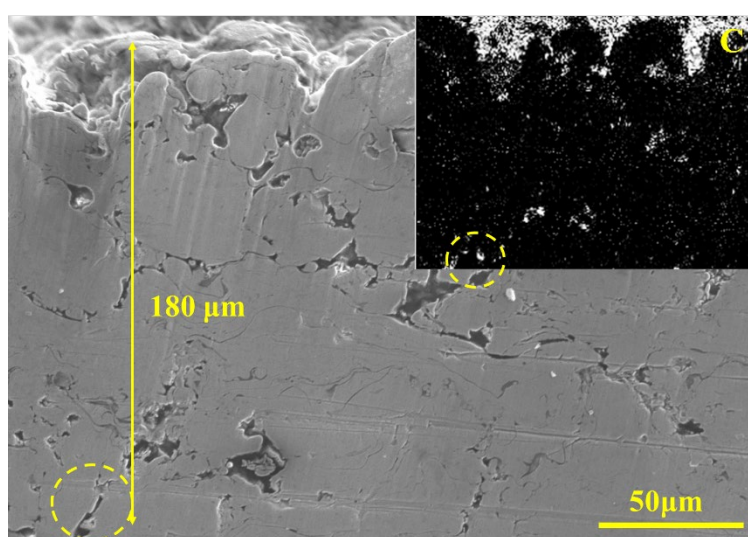


**Fig.6.** The SEM image of the cross-section of the MoS<sub>2</sub>/WBS-ACR@HEA coating and the corresponding EDX mapping image.

### 3.3 The thermal stability of the synthetic sealant powders

The thermal stability of sealants is an important parameter for evaluating their service performance in harsh environments. Fig. 7 presents the TGA curves of the MoS<sub>2</sub>, WBS-ACR and MoS<sub>2</sub>/WBS-ACR composite powders under air atmosphere. When the temperature increased to 800 °C, the total mass loss of the pure MoS<sub>2</sub> was about 13%, which is close to the weight loss of SO<sub>2</sub> (10%) produced by the thermal decomposition of MoS<sub>2</sub> [26]. The extra 3% weight loss could be attributed to the release of the absorbed water in ambient atmosphere. The thermal decomposition of WBS-ACR and MoS<sub>2</sub>/WBS-ACR composite shown in Fig.7 can be split into two stages. Up to 320 °C, the mass loss of about 20% could be assumed to be due to the volatilization of physisorbed water and the primary decomposition of the resin [39]. When the temperature rises to 320 °C, the TGA curves show a rapid downward trend, resulting from the dehydration in the polymer chains and the decomposition of WBS-ACR. The flatter curve and less weight loss of MoS<sub>2</sub>/WBS-ACR composite ranging in 320-420°C indicates the introduction of MoS<sub>2</sub> could retard the thermal degradation of WBS-ACR. The improved thermal stability could be benefitting from the 2D layered structure of MoS<sub>2</sub>, which not only reduces heat conduction but also limits the movement of polymer chains [22, 26].

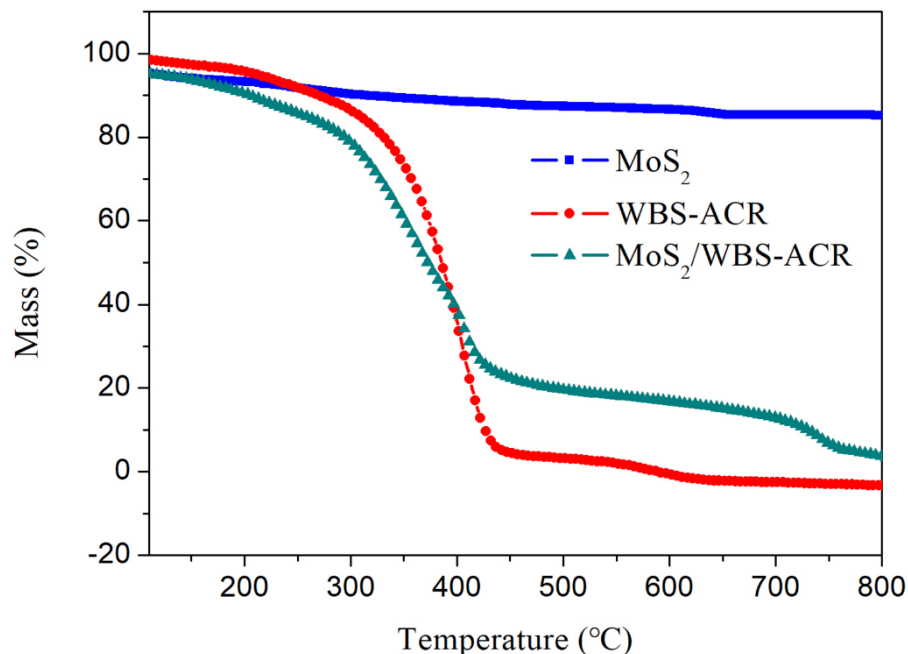


**Fig.7.** TGA diagram of MoS<sub>2</sub>, WBS-ACR and MoS<sub>2</sub>/WBS-ACR composite powders.

### 3.4 Tribological properties of the HEA coatings with sealing treatment

The comparison of the friction coefficient as a function of sliding time for the as-

sprayed and sealed HEA coatings is shown in Fig. 8a. Obviously, the friction coefficient of the as-sprayed HEA coating increases rapidly at the beginning of sliding friction and ultimately stabilizes above 0.4. The friction coefficient of the WBS-ACR@HEA coating shows the similar variation trend to the as-sprayed HEA coating, but the value is always lower in the whole sliding process, indicating the lubricating effect of the introduced WBS-ACR sealant. It is noteworthy that the changing trend of friction coefficient with cycles of the MoS<sub>2</sub>@HEA coating and the MoS<sub>2</sub>/WBS-ACR@HEA coating is totally different to the coatings without MoS<sub>2</sub>. From the start of the test the friction coefficient of both the coatings showed steady and lower values at about 0.15 and 0.19 for MoS<sub>2</sub>@HEA coating and the MoS<sub>2</sub>/WBS-ACR@HEA, respectively. Therefore, it is reasonable to believe that the introduced MoS<sub>2</sub> by hydrothermal reaction can effectively reduce the friction coefficient of the coating. This result is consistent with the literature, which used various methods to introduce MoS<sub>2</sub> into thermal spray coatings to improve the tribological properties [45-48]. To further investigate the effect of sealants on the tribological properties of HEA coatings, the wear rates of the as-sprayed and sealed HEA coatings are shown in Fig 8b. This result shows the similar changing trend with that of friction coefficient. Apparently, the WBS-ACR@HEA coating presents lower wear rate than that of as-sprayed HEA coatings, while the MoS<sub>2</sub>@HEA coating and MoS<sub>2</sub>/WBS-ACR@HEA coating has the similarly lowest wear rate of about  $9.2 \times 10^{-5} \text{ mm}^3/\text{Nm}$ . This indicates that the presence of MoS<sub>2</sub> can also significantly improve the wear resistance of the HEA coatings.

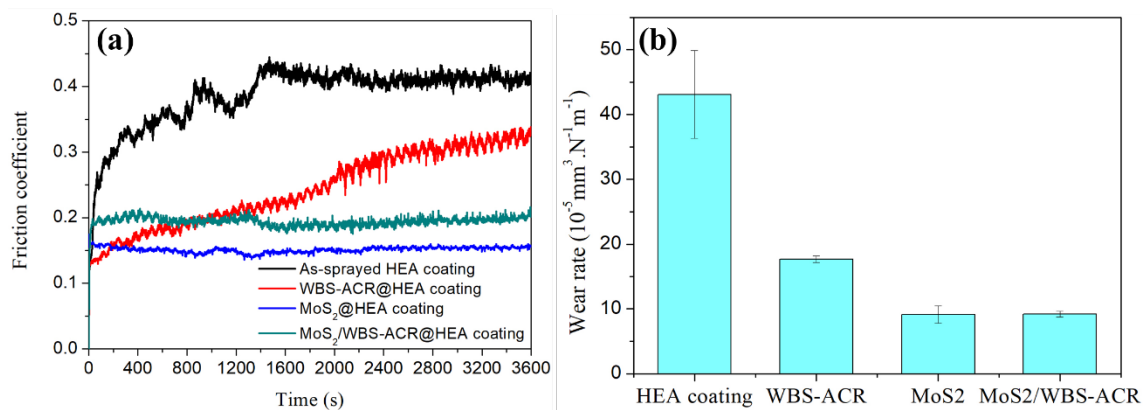


**Fig.8.** (a) The friction coefficient and (b) the corresponding wear rate of the as-sprayed and sealed HEA coatings.

Fig.9 shows the worn morphologies and the corresponding 3D profiles of the wear tracks for the as-sprayed and sealed HEA coatings. Some large adhesive blocks and cracks can be clearly observed on the worn surface of the untreated HEA coating (Fig. 9a). The adhesive blocks detected by EDX (Fig. 10a) are mainly composed of oxide



and aluminum oxide, indicating that the adhesive wear and oxidative wear occurred in the sliding friction. The cracks mainly propagated outward from the intrinsic defects and pores in Fig 9a, induced by the stress concentration under the applied normal load. The numerous micro-defects in the untreated HEA coating could act as the nucleation sites for the generation of new cracks, which will gradually to grow and merge, ultimately leading to the peeling of the coating under the continuous wear process [49, 50]. The severe adhesive wear and coating delamination result in high wear rate of the as-sprayed HEA coating. Although there are still some significant adhesive blocks on the worn surface, the cracks on the worn surface of the WBS-ACR@HEA coating are significantly reduced (Fig. 7b). The filling of the polymeric sealant in intrinsic defects could significantly improve the load-bearing capacity of the HEA coating, which prevents the further propagation of the micro-cracks and relieves the delamination of the coating. Besides, the decreased wear rate of the WBS-ACR@HEA coating could also be attributed to the lubricating effect of the polymeric sealant, which has been observed in previous studies [51, 52].

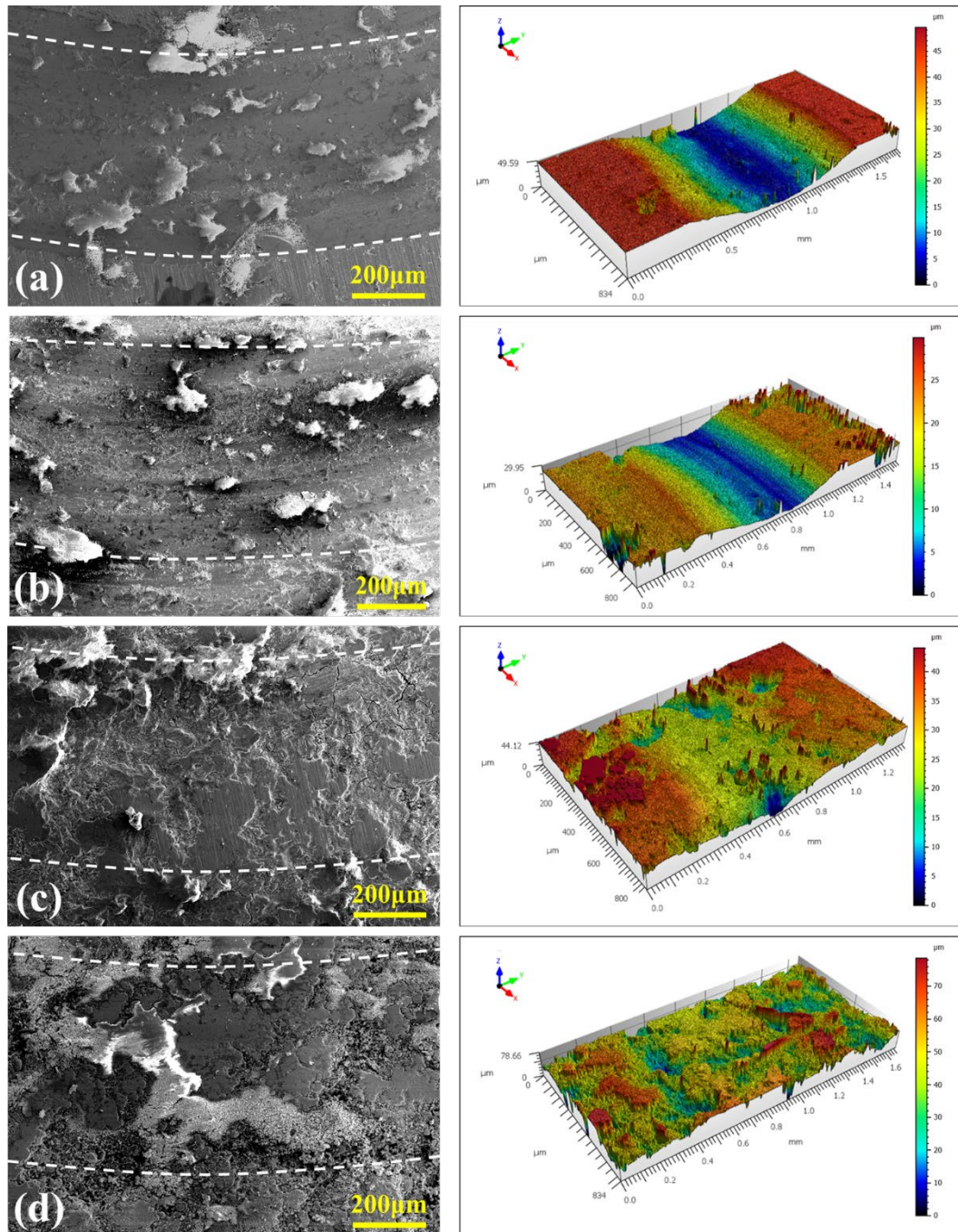


**Fig. 9.** The worn morphologies and the corresponding 3D profiles of the wear tracks for (a) the as-sprayed, (b) WBS-ACR@HEA coating, (c) MoS<sub>2</sub>@HEA coating and (d) MoS<sub>2</sub>/WBS-ACR@HEA coating.

Interestingly, the worn morphologies of the MoS<sub>2</sub>@HEA coating and MoS<sub>2</sub>/WBS-ACR@HEA coating (Fig. 9c&d) exhibit a distinct and noteworthy appearance with most of the worn surface being smooth and dense without obvious worn particles and cracks. The wear depth in the 3D profiles of the wear tracks is significantly shallower, indicating very slight wear on the MoS<sub>2</sub>@HEA coating and MoS<sub>2</sub>/WBS-ACR@HEA coating. Besides, it can be observed that there are two different components distributed

on both the worn surfaces, corresponding to the coating phase and the sealant phase, respectively. This finding could be further verified by the EDS analysis (Fig. 10 b&c). The synthesized solid lubricants of MoS<sub>2</sub> in the pores could form a self-lubricating layer on the contact surface, which separated the HEA coating from the ZrO<sub>2</sub> counterpart effectively during the sliding friction, thereby reducing the friction coefficient and wear rate significantly [16, 18, 19, 23]. It should be mentioned that there is still a large reservoir of sealant containing MoS<sub>2</sub> stored in the pores of the coatings, which can continuously provide lubricating particles for frictional contact, achieving long-term lubrication of the coatings. Therefore, it can be concluded that the introduction of MoS<sub>2</sub> into the sealants could efficiently improve the tribological performance of the as-sprayed HEA coatings.

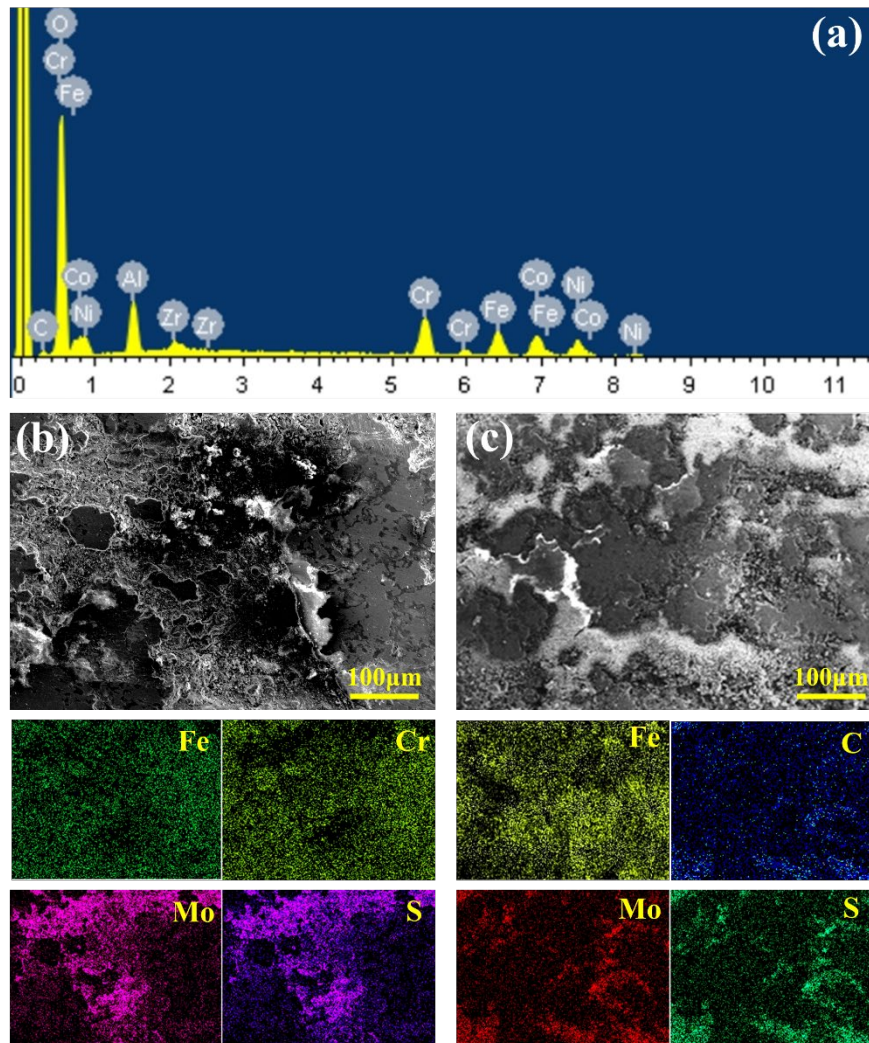


**Fig. 10.** (a) The EDX spectrum of the adhesive blocks on the worn surface of the HEA coating, and localized magnified wear morphology and corresponding element mapping of (a) MoS<sub>2</sub>@HEA coating and (b) MoS<sub>2</sub>/WBS-ACR@HEA coating.



### 3.5 Anti-corrosion performance of the HEA coatings with sealing treatment

In order to reveal the effect of the as-prepared sealants on the corrosion protection of plasma sprayed HEA coatings, the polarization curves of HEA coating, MoS<sub>2</sub>@HEA coating, WBS-ACR@HEA coating and MoS<sub>2</sub>/WBS-ACR@HEA coatings in 3.5 wt% NaCl solution are shown in Fig. 11a, and the corresponding corrosion potential ( $E_{\text{corr}}$ ) and corrosion current density ( $i_{\text{corr}}$ ) are plotted in Fig. 11b. In general, the more positive the corrosion potential and the smaller the corrosion current, the better the corrosion resistance [22]. It is clearly found that the  $E_{\text{corr}}$  value of WBS-ACR@HEA coating and MoS<sub>2</sub>/WBS-ACR@HEA coatings is -0.48 V and -0.50 V in sequence, more positive than that of as-sprayed HEA coating (-0.81 V). Furthermore, the  $i_{\text{corr}}$  of WBS-ACR@HEA coating and MoS<sub>2</sub>/WBS-ACR@HEA coatings is  $4.8 \times 10^{-6}$  A/cm<sup>2</sup> and  $1.1 \times 10^{-6}$  A/cm<sup>2</sup>, which is less than one order of magnitude than that of HEA coating ( $2.7 \times 10^{-5}$  A/cm<sup>2</sup>). The results of polarization curves indicate that the WBS-ACR and MoS<sub>2</sub>/WBS-ACR composite material can effectively seal the defects and pores in the as-sprayed coatings, improving the anti-corrosion performance. Interestingly, it is worth noting that the corrosion potential of MoS<sub>2</sub>@HEA coating exhibits negative displacement relative to the HEA coating, while the  $i_{\text{corr}}$  shows a higher value of  $1.6 \times 10^{-4}$  A/cm<sup>2</sup>, indicating that the addition of pure MoS<sub>2</sub> deteriorates the corrosion resistance of the HEA coating.

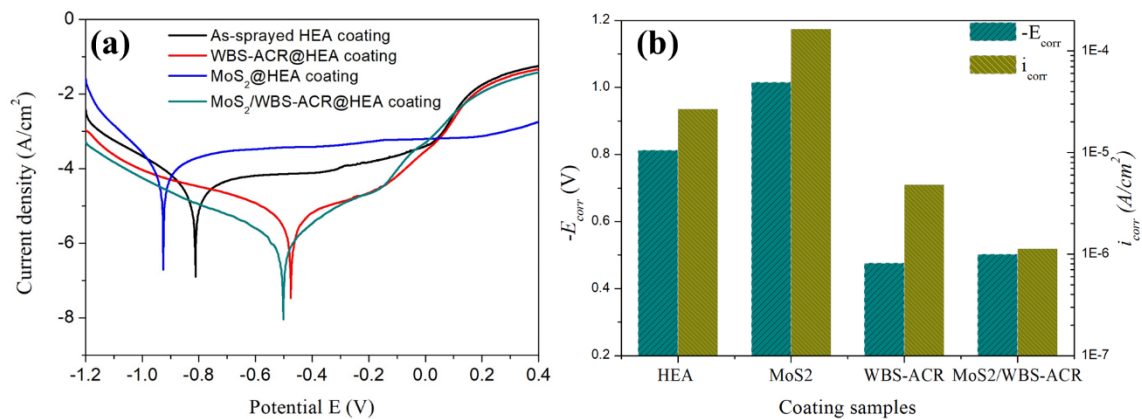


**Fig.11.** (a) Polarization curves of as-sprayed and sealed HEA coatings in 3.5 wt% NaCl solution, (b) the corresponding corrosion potential and corrosion current density.

To further understand the electrochemical properties of the HEA coatings treated with the as-prepared sealants, the electrochemical impedance spectroscopy (EIS) and the fitting results are shown in Fig.12. The Nyquist plots (Fig. 12a) reveal different electrochemical behavior for the as-sprayed and sealed HEA coatings in 3.5 wt% NaCl solution. The larger diameter of capacitive arc in the Nyquist plots generally represent the greater impedance value and the better corrosion resistance [40]. Clearly, the WBS-

ACR@HEA coating and MoS<sub>2</sub>/WBS-ACR@HEA coating exhibit higher values of imaginary and real components than that of HEA coating, suggesting better corrosion resistance. Similarly, compared to the HEA coating, the MoS<sub>2</sub>@HEA coating shows lower radius of the capacitance arcs, indicating the worse charge transfer resistance to prevent the penetration of corrosive media [53]. The Bode plots in Fig. 12b also present obvious difference among the individual samples, in which the larger impedance value at low frequency reflects the better corrosion resistance of the coatings [54]. The impedance modulus of WBS-ACR@HEA coating and MoS<sub>2</sub>/WBS-ACR@HEA coating at low-frequency of 0.01 Hz is not very different, being 35 kΩ.cm<sup>2</sup> and 30 kΩ.cm<sup>2</sup> respectively. The values are one and two order of magnitude higher than that of HEA coating (3 kΩ.cm<sup>2</sup>) and MoS<sub>2</sub>@HEA coating (0.3 kΩ.cm<sup>2</sup>), confirming the better anti-corrosion ability of the WBS-ACR and MoS<sub>2</sub>/WBS-ACR composite sealants due to the shielding effect of corrosive media by the uniform and compact microstructure [39].

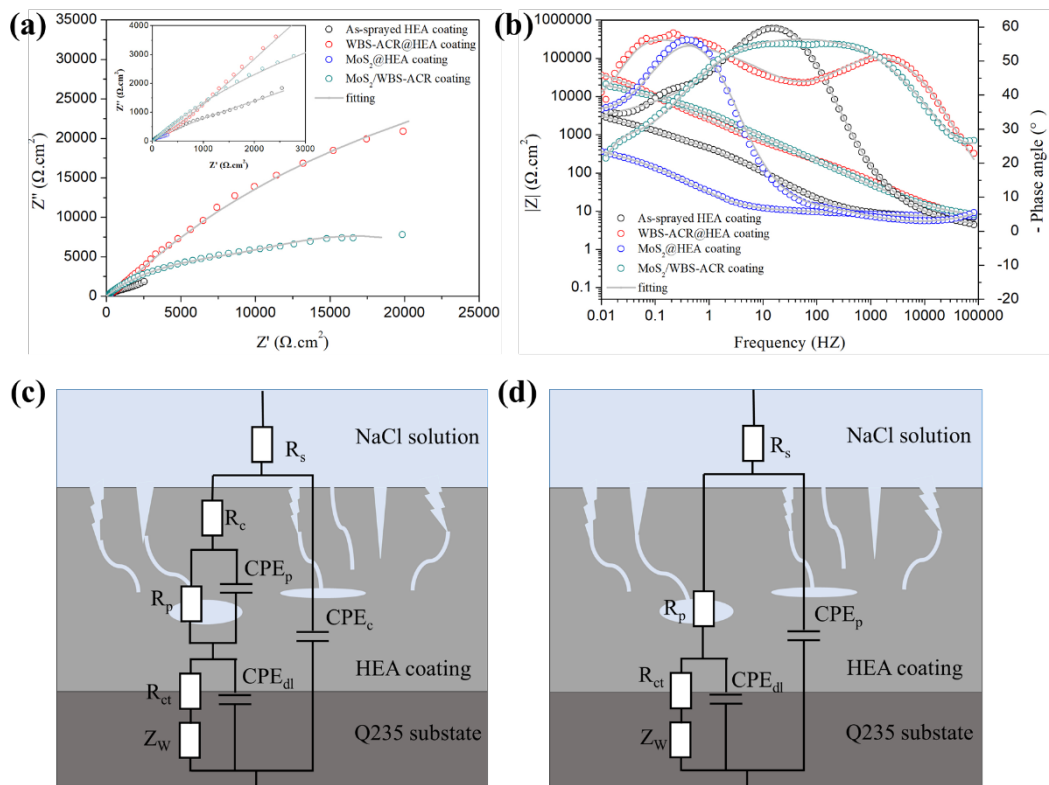


**Fig.12.** Electrochemical plots of the as-sprayed and sealed HEA coatings: (a) Nyquist plots, (b) Bode and phase plots, and (c, d) the corresponding electrical equivalent circuits.

**Table 5.** Tafel electrochemical measurement data.

	$R_s$ ( $\Omega/\text{cm}^2$ )	$R_c$ ( $\Omega/\text{cm}^2$ )	$R_p$ ( $\Omega/\text{cm}^2$ )	$R_{ct}$ ( $\Omega/\text{cm}^2$ )	chi-squared
HEA	6.6	0.02	520	545	$2.1 \times 10^{-4}$
MoS <sub>2</sub> @HEA	0.1	7.8	2.9	227	$5.8 \times 10^{-4}$
WBS-ACR@HEA	5.7	344	$1.9 \times 10^4$	$1.9 \times 10^4$	$6.5 \times 10^{-4}$
MoS <sub>2</sub> /WBS-ACR@HEA	6.1	/	$1.8 \times 10^4$	9752	$4.6 \times 10^{-4}$

The electrical equivalent circuits employed to fit the EIS data were shown in Fig 12 c&d. In Table 5,  $R_s$ ,  $R_c$ ,  $R_p$  and  $R_{ct}$  represent the solution resistance, coating resistance, pore resistance and interfacial charge transfer resistance, respectively. Considering the ideality of the system, CPE (constant phase element) and  $Z_w$  was added to replace the corresponded capacitors and Warburg impedance. The fitting results of the as-sprayed and the sealed HEA coatings are exhibited in Table 3. The chi-squares of all fittings are in the magnitude order of  $10^{-4}$ , which indicates a high degree of fitting and reliable fitting parameters.

During the plasma spraying process, pores and micro-defects inevitably appeared in the HEA coatings due to the staggered stacking of numerous flat particles, oxides, and completely or partially unmelted particles [4, 5, 37]. When the as-sprayed HEA coating is working in a corrosive environment, corrosive media such as air and water can reach the interface between the substrate and the coating through interconnected pores, causing serious corrosion to the substrate. This result is consistent with the low value of  $R_p$  ( $520 \text{ } (\Omega/\text{cm}^2)$ ). When the WBS-ACR and MoS<sub>2</sub>/WBS-ACR sealants were introduced to fill the pores and micro-defects of the HEA coatings, the compact microstructure of the sealants reduced the pore defects effectively, which greatly improved the propagation path of the corrosive medium to the substrate. The  $R_p$  value of WBS-ACR@HEA and MoS<sub>2</sub>/WBS-ACR@HEA coatings therefore shows a significant improvement to  $1.9 \times 10^4 \text{ } \Omega/\text{cm}^2$  and  $1.8 \times 10^4 \text{ } \Omega/\text{cm}^2$ , respectively.

Interestingly,  $R_p$  of the MoS<sub>2</sub>@HEA is two orders of magnitude lower than that of the HEA coating. During the preparation of the MoS<sub>2</sub>@HEA coating, the precursors of CS(NH<sub>2</sub>)<sub>2</sub> and Na<sub>2</sub>MoO<sub>4</sub> were first introduced into the pores of HEA coating through ultrasound and vacuum impregnation. During the hydrothermal process, thiourea will further hydrolyze to produce H<sub>2</sub>S and CO<sub>2</sub>. The acid gases dissolved in water may react with the HEA coating, resulting in more serious destruction of coating pores and worse

corrosion resistance. Besides, the XRD result indicates that the phase structure of synthesized MoS<sub>2</sub> is consistent with that of 1T-MoS<sub>2</sub>. However, 1T-MoS<sub>2</sub> has better conductivity due to its metallic properties, which will greatly accelerate electron transfer during the corrosion process [28, 29]. This result can be shown by the lowest R<sub>ct</sub> of about 227 Ω/cm<sup>2</sup> for the MoS<sub>2</sub>@HEA coating. The conductive MoS<sub>2</sub> nanoparticles may form a bridge between the substrate and the coating, leading to the occurrence of “micro galvanic corrosion”. Compared to WBS-ACR@HEA coating, the slightly decreased R<sub>ct</sub> of MoS<sub>2</sub>/WBS-ACR@HEA coating may also be attributed to the enhanced charge transfer capacity of MoS<sub>2</sub>.

#### 4. Conclusion

In summary, MoS<sub>2</sub>/WBS-ACR hybrid sealant was successfully prepared in the pores and micro-defects of plasma sprayed HEA coatings by in-situ hydrothermal reaction. The filling effect, thermal stability, tribological and anti-corrosion performance of HEA coatings sealed with hybrid sealant were evaluated systematically with the comparison of as-sprayed HEA coating and HEA coatings sealed with MoS<sub>2</sub> and WBS-ACR only. The mechanism of improved wear and corrosion resistance for MoS<sub>2</sub>/WBS-ACR hybrid sealants was also discussed in detail. The main conclusions were as follows:

- (1) MoS<sub>2</sub> synthesized by the hydrothermal reaction of precursor solution are uniformly dispersed in the WBS-ACR matrix without obvious agglomeration. The filling layers of MoS<sub>2</sub>/WBS-ACR hybrid sealant exhibit good adhesion to the HEA coating with smooth and compact microstructure, while the maximum penetration depth exceeds 180 μm, indicating outstanding sealing effect.
- (2) The introduction of MoS<sub>2</sub> into the WBS-ACR matrix significantly reduce the friction coefficient and improves the wear resistance of HEA coatings, attributing to the formation of MoS<sub>2</sub> lubricating layers in the wear track, and the suppression of micro-crack propagation from the intrinsic pores and defects.
- (3) Compared to the deterioration of corrosion resistance of HEA coatings caused by MoS<sub>2</sub> filling, the MoS<sub>2</sub>/WBS-ACR hybrid sealant fully inherit the excellent anti-corrosion performance of resin materials by reducing the pore defects efficaciously and improving the propagation path of the corrosive medium to the substrate.
- (4) The successful preparation of MoS<sub>2</sub>/WBS-ACR sealant provides new ideas for the development of sealant materials, transforming from a single improvement in corrosion resistance to a multifunctional synergistic enhancement. It also provides new potential for the application of thermal spray coatings in extreme environment.

## Acknowledgments

The authors gratefully acknowledge the financial support from the Fundamental Research Funds for the Central Universities, China (Grant No: B220202037), the Natural Science Foundation of Jiangsu Province of China (BK20210374), and the Doctoral Program of Entrepreneurship and Innovation of Jiangsu Province (JSSCBS20210254).

## Declaration of Competing Interest

There are no conflicts to declare.

## Author Contributions

**Xiangru Shi:** Conceptualization, Supervision, Investigation, Formal analysis, Funding acquisition, Writing - Original Draft. **Ming Liu:** Investigation, Methodology, Resources, Data Curation. **Peihua He:** Investigation, Methodology. **Jian Chen:** Methodology, Resources, Writing - Review & Editing. **Ben D. Beake:** Writing - Review & Editing. **Tomasz W. Liskiewicz:** Writing - Review & Editing. **Jiangbo Chen:** Writing - Review & Editing.

## References:

- [1] S. Alvi, D.M. Jarzabek, M.G. Kohan, D. Hedman, F. Akhtar, Synthesis and mechanical characterization of a CuMoTaWV high-entropy film by magnetron sputtering, *ACS Applied Materials & Interfaces*, 12(2020).
- [2] G. Jin, Z. Cai, Y. Guan, X. Cui, Z. Liu, Y. Li, M. Dong, D. Zhang, High temperature wear performance of laser-cladded FeNiCoAlCu high-entropy alloy coating, *Applied Surface Science*, 445(2018) 113-122.
- [3] C. Oses, C. Toher, S. Curtarolo, High-entropy ceramics, *Nature Reviews Materials*, 5(2020) 295–309.
- [4] L. Chen, K. Bobzin, Z. Zhou, L. Zhao, M. Öte, T. Königstein, Z. Tan, D. He, Wear behavior of HVOF-sprayed Al<sub>0.6</sub>TiCrFeCoNi high entropy alloy coatings at different temperatures, *Surface and Coatings Technology*, 358(2019) 215-222.
- [5] R. Bhaskaran Nair, R. Supekar, S. Morteza Javid, W. Wang, Y. Zou, A. McDonald, J. Mostaghimi, P. Stoyanov, High-Entropy Alloy Coatings Deposited by Thermal Spraying: A Review of Strengthening Mechanisms, Performance Assessments and Perspectives on Future Applications, *Metals*, 13(2023) 579.
- [6] A. Sharma, High Entropy Alloy Coatings and Technology, *Coatings*, 11(2021) 372.
- [7] A. Meghwal, A. Anupam, C. Schulz, C. Hall, B.S. Murty, R.S. Kottada, R. Vijay, P. Munroe, C.C. Berndt, A.S.M. Ang, Tribological and corrosion performance of an atmospheric plasma sprayed AlCoCr<sub>0.5</sub>Ni high-entropy alloy coating, *Wear*, 506-507(2022) 204443.
- [8] Y. Wang, C.M. Wu, W. Li, H.Y. Li, Y.C. Li, X.Y. Zhang, L.L. Sun, Effect of bionic hydrophobic structures on the corrosion performance of Fe-based amorphous metallic coatings, *Surface and*



Coatings Technology, 416(2021) 127176.

- [9] L. Sopchenski, J. Robert, M. Touzin, A. Tricoteaux, M. Olivier, Improvement of wear and corrosion protection of PEO on AA2024 via sol-gel sealing, *Surface and Coatings Technology*, 417(2021) 127195.
- [10] Y. Tian, H. Zhang, X. Chen, A. McDonald, S. Wu, T. Xiao, H. Li, Effect of cavitation on corrosion behavior of HVOF-sprayed WC-10Co4Cr coating with post-sealing in artificial seawater, *Surface and Coatings Technology*, 397(2020) 126012.
- [11] S. Ahmaniemi, M. Vippola, P. Vuoristo, T. Mäntylä, M. Buchmann, R. Gadov, Residual stresses in aluminium phosphate sealed plasma sprayed oxide coatings and their effect on abrasive wear, *Wear*, 252(2002) 614-623
- [12] S. Liscano, L. Gil, M.H. Staia, Correlation between microstructural characteristics and the abrasion wear resistance of sealed thermal-sprayed coatings, *Surface and Coatings Technology*, 200(2005) 1310-1314.
- [13] P. Feng, S. Shen, L. Yang, Y. Kong, S. Yang, C. Shuai, Vertical and uniform growth of MoS<sub>2</sub> nanosheets on GO nanosheets for efficient mechanical reinforcement in polymer scaffold, *Virtual and Physical Prototyping*, 18(2023).
- [14] D. Mouloua, A. Kotbi, G. Deokar, K. Kaja, M. El Marssi, M.A. EL Khakani, M. Jouiad, Recent Progress in the Synthesis of MoS<sub>2</sub> Thin Films for Sensing, Photovoltaic and Plasmonic Applications: A Review, *Materials*, 14(2021) 3283.
- [15] R.B. Pujari, A.C. Lokhande, A.R. Shelke, J.H. Kim, C.D. Lokhande, Chemically deposited nano grain composed MoS<sub>2</sub> thin films for supercapacitor application, *Journal of Colloid and Interface Science*, 496(2017) 1-7.
- [16] Z. Chen, D. Liu, L. Ren, C. Zhang, H. Huang, Hydrothermal Synthesis of MoS<sub>2</sub> into Flame-Sprayed Ni60 Coating towards Superior Tribological Performance, *Journal of Materials Engineering and Performance*, (2022).
- [17] A.A. Burkov, S.V. Nikolenko, P.G. Chigrin, M.A. Kulik, V.O. Krutikova, A.A. Karpenko, Liquid-phase hydrothermal deposition of MoS<sub>2</sub> into TiAl coatings on Ti6Al4V alloy, *Surface and Coatings Technology*, 421(2021) 127379.
- [18] S. Li, X. Zhao, Y. An, D. Liu, H. Zhou, J. Chen, YSZ/MoS<sub>2</sub> self-lubricating coating fabricated by thermal spraying and hydrothermal reaction, *Ceramics International*, 44(2018) 17864-17872.
- [19] W. Deng, X. Zhao, Y. An, E. Hao, S. Li, H. Zhou, J. Chen, Improvement of tribological properties of as-sprayed 8YSZ coatings by in-situ synthesis C/MoS<sub>2</sub> composite lubricant, *Tribology International*, 128(2018) 260-270.
- [20] W. Deng, S. Li, X. Liu, X. Zhao, Y. An, H. Zhou, J. Chen, A novel approach to fabricate hybrid materials with excellent tribological properties from spray-formed ceramic, *Materials Letters*, 193(2017) 199-202.
- [21] W. He, Z. Zhang, R. Wang, Y. Zhang, Q. Wang, T. Wang, X. Pei, Effect of core-shell structured SiO<sub>2</sub>@MoS<sub>2</sub> on the tribological properties of epoxy resin/carboxyl terminated butadiene acrylonitrile composites, *Polymer Composites*, 44(2023) 1252-1263.
- [22] X. Li, X. Liu, H. Liu, X. Liu, R. He, S. Meng, Structure, morphology and anti-corrosion performance of polyaniline modified molybdenum sulfide/epoxy composite coating, *Colloids and Surfaces A: Physicochemical and Engineering Aspects*, 639(2022) 128345.
- [23] Q. Lin, X. Wang, M. Cai, H. Yan, Z. Zhao, X. Fan, M. Zhu, Enhancement of Si<sub>3</sub>N<sub>4</sub>@MoS<sub>2</sub> core-shell structure on wear/corrosion resistance of epoxy resin/polyacrylate IPN composite coating,

Applied Surface Science, 568(2021) 150938.

- [24] Z. Xia, G. Liu, Y. Dong, Y. Zhang, Anticorrosive epoxy coatings based on polydopamine modified molybdenum disulfide, *Progress in Organic Coatings*, 133(2019) 154-160.
- [25] R. Ahmad, R. Srivastava, S. Yadav, S. Chand, and S. Sapra, Functionalized 2D-MoS<sub>2</sub>-Incorporated Polymer Ternary Solar Cells: Role of Nanosheet-Induced Long-Range Ordering of Polymer Chains on Charge Transport, *ACS Applied Materials & Interfaces*, 9 (2017) 34111-34121.
- [26] K. Zhou, S. Jiang, C. Bao, L. Song, B. Wang, G. Tang, Y. Hu, Z. Gui, Preparation of poly(vinyl alcohol) nanocomposites with molybdenum disulfide (MoS<sub>2</sub>): structural characteristics and markedly enhanced properties, *RSC Advances*, 2(2012) 11695-11703.
- [27] Z. Li, R. Fan, Z. Hu, W. Li, H. Zhou, S. Kang, Y. Zhang, H. Zhang, G. Wang, Ethanol introduced synthesis of ultrastable 1T-MoS<sub>2</sub> for removal of Cr(VI), *Journal of Hazardous Materials*, 394(2020) 122525.
- [28] X. Wang, H. Li, H. Li, S. Lin, W. Ding, X. Zhu, Z. Sheng, H. Wang, X. Zhu, Y. Sun, 2D/2D 1T - MoS<sub>2</sub>/Ti<sub>3</sub>C<sub>2</sub> MXene Heterostructure with Excellent Supercapacitor Performance, *Advanced Functional Materials*, 30(2020) 190302.
- [29] W. Ding, L. Hu, J. Dai, X. Tang, R. Wei, Z. Sheng, C. Liang, D. Shao, W. Song, Q. Liu, M. Chen, X. Zhu, S. Chou, X. Zhu, Q. Chen, Y. Sun, S.X. Dou, Highly Ambient-Stable 1T-MoS<sub>2</sub> and 1T-WS<sub>2</sub> by Hydrothermal Synthesis under High Magnetic Fields, *ACS Nano*, (2019).
- [30] M. Acerce, D. Voiry, M. Chhowalla, Metallic 1T phase MoS<sub>2</sub> nanosheets as supercapacitor electrode materials, *Nature Nanotechnology*, 10(2015) 313-318.
- [31] E. Ghaleghafi, M.B. Rahmani, Exploring different routes for the synthesis of 2D MoS<sub>2</sub>/1D PANI nanocomposites and investigating their electrical properties, *Physica E: Low-dimensional Systems and Nanostructures*, 138(2022) 115128.
- [32] S. Saha, N. Chaudhary, H. Mittal, G. Gupta, M. Khanuja, Inorganic - organic nanohybrid of MoS<sub>2</sub>-PANI for advanced photocatalytic application, *International Nano Letters*, 9(2019) 127-139.
- [33] X. Zhang, L. Ma, M. Gan, G. Fu, M. Jin, Y. Zhai, Controllable constructing of hollow MoS<sub>2</sub>/PANI core/shell microsphere for energy storage, *Applied Surface Science*, 460(2018) 48-57.
- [34] H. Song, B. Wang, Q. Zhou, J. Xiao, X. Jia, Preparation and tribological properties of MoS<sub>2</sub>/graphene oxide composites, *Applied Surface Science*, 419(2017) 24-34.
- [35] H. Lei, D. He, Y. Guo, Y. Tang, H. Huang, Synthesis and characterization of UV-absorbing fluorine-silicone acrylic resin polymer, *Applied Surface Science*, 442(2018) 71-77.
- [36] B. Zhu, Z. Liu, J. Liu, Y. Yang, Y. Meng, F. Yu, L. Jiang, G. Wei, Z. Zhang, Preparation of fluorinated/silanized polyacrylates amphiphilic polymers and their anticorrosion and antifouling performance, *Progress in Organic Coatings*, 140(2020) 105510.
- [37] J. Lu, Y. Chen, Z. Sun, L. Li, X. Liu, A. Huang, H. Zhang, F. Guo, X. Zhang, X. Zhao, Air plasma sprayed high-entropy AlCoCrFeNiY coating with excellent oxidation and spallation resistance under cyclic oxidation at 1050 - 1150 °C, *Corrosion Science*, 198(2022) 110151.
- [38] J.G. Odhiambo, W. Li, Y. Zhao, C. Li, Porosity and Its Significance in Plasma-Sprayed Coatings, *Coatings*, 9(2019) 460.
- [39] G. Wang, Z. Zhou, Q. Hu, X. Shi, X. Zhang, K. Zhang, L. Wu, Preparation of eco-friendly natural rosin-based SiO<sub>2</sub>-NH<sub>2</sub>@GO hybrid sealant and study on corrosion resistance of Fe-based amorphous coating for steel substrate, *Carbon*, 201(2023) 170-188.
- [40] J. Huang, D. Zhao, Y. Gong, C. Yang, H. Zhu, M. Wang, D. Chen, H. Wang, Improved corrosion resistance of PEO-coated 7085Al alloy via a novel organic and inorganic sealing-treatment

- combination, *Surface and Coatings Technology*, 441(2022) 128566.
- [41] M. Liu, Z. Wang, H. Hu, L. Zhang, Y. Zheng, Effect of Sealing Treatments on Erosion – Corrosion of a Fe-Based Amorphous Metallic Coating in 3.5 wt.% NaCl Solution with 2 wt.% Sand, *Metals*, 12(2022) 680.
- [42] R. Westergård, S. Hogmark, Sealing to improve the wear properties of plasma sprayed alumina by electro-deposited Ni, *Wear*, 256(2004) 1153-1162.
- [43] L.M. Zhang, S.D. Zhang, A.L. Ma, H.X. Hu, Y.G. Zheng, B.J. Yang, J.Q. Wang, Influence of sealing treatment on the corrosion behavior of HVAF sprayed Al-based amorphous/nanocrystalline coating, *Surface and Coatings Technology*, 353(2018) 11.
- [44] H.P. Thi, T.N. Van, T.A. Nguyen, Q. Le Thu, L.P. Thi, T.D. Bich, T.T. Van, C.L. Quoc, Cr<sub>3</sub>C<sub>2</sub>-25NiCr Cermet Coating: Preparation, PTFE Sealant, Wear and Corrosion Resistances, *Journal of Thermal Spray Technology*, 30(2021) 716-724.
- [45] D. Kopp, J.M. Lackner, R. Kaindl, R. Elter, M. Stummer, A. Hinterer, A.M. Coclite, W. Waldhauser, Low-friction, wear-protecting coatings on polymers by atmospheric pressure plasma spraying, *Surface and Coatings Technology*, 448(2022) 128930.
- [46] Z. Wu, S. Li, P. Zhang, C. Wang, C. Deng, J. Mao, W. Li, X. Tu, Controllable in-situ synthesis of MoS<sub>2</sub>/C in plasma-sprayed YSZ coatings: Microstructure, mechanical and tribological properties, *Surface and Coatings Technology*, 448(2022) 128895.
- [47] C. Satish, K. Vijay Kumar, S. Prasad, P. Sai Kiran, O.S. Asiq Rahman, P. Singh, S. Indupuri, R. Shrivastava, S.M. Pandey, A.K. Keshri, Effect of Al<sub>2</sub>O<sub>3</sub> and MoS<sub>2</sub> reinforcement on microstructure, mechanical, and wear properties of plasma sprayed aluminium hybrid composite coating, *Materials Today Communications*, 36(2023) 106640.
- [48] R.K.S. Gautam, U.S. Rao, R. Tyagi, Influence of Load on Friction and Wear Behavior of Ni-Based Self-Lubricating Coatings Deposited by Atmospheric Plasma Spray, *Journal of Materials Engineering and Performance*, 28(2019) 7398-7406.
- [49] Q. Wang, S. Tu, Y. Rao, R. Chidambaram Seshadri, The Influence of Polymeric Sealing Treatment on the Wear Performance of PEO Coating Deposited on AZ31 Mg Alloy, *Coatings*, 12(2022) 182.
- [50] Q. Wang, C.S. Ramachandran, G.M. Smith, S. Sampath, Sliding wear behavior of air plasma sprayed Al<sub>2</sub>O<sub>3</sub> coatings sealed with aluminum phosphate, *Tribology International*, 116(2017) 431-439.
- [51] G. Wang, Z. Zhou, K. Zhang, L. Wu, X. Shi, X. Zhang, Effect of eco-friendly rosin sealant on wear resistance of Fe-based amorphous coating, *Materials Letters*, 349(2023) 134855.
- [52] Y. Wan, Y. Yu, L. Cao, M. Zhang, J. Gao, C. Qi, Corrosion and tribological performance of PTFE-coated electroless nickel boron coatings, *Surface and Coatings Technology*, 307(2016) 316-323.
- [53] G. Liu, S.G. Zhou, Q.F. Li, C. Wang, J.W. Zhang, J.P. Liu, Effect of MoS<sub>2</sub> on tribological properties and corrosion resistance of MoS<sub>2</sub>/a-C:H films fabricated via reactive magnetron sputtering technology, *Materials Research Express*, 6(2019).
- [54] Z. Yang, L. Wang, W. Sun, S. Li, T. Zhu, W. Liu, G. Liu, Superhydrophobic epoxy coating modified by fluorographene used for anti-corrosion and self-cleaning, *Applied Surface Science*, 401(2017) 146-155.